UHASSELT
KNOWLEDGE IN ACTION

Maastricht University

Faculty of Medicine and Life Sciences
School for Life Sciences
Master of Biomedical Sciences

Master's thesis

Conductive MXene-based bioink for integrating biomimetic electronics into new 3D skin model

Yana Heyvaert

Thesis presented in fulfillment of the requirements for the degree of Master of Biomedical Sciences, specialization Bioelectronics and Nanotechnology

SUPERVISOR :
Prof. dr. Anitha ETHIRAJAN

SUPERVISOR :
Prof. dr. Roman ANTONANZAS PEREZ

CO-SUPERVISOR :
Prof. Dr. Miguel Angel MATEOS TIMONEDA

MENTOR :
Dhr. Maximilian JERGITSCH

2023
2024

Transnational University Limburg is a unique collaboration of two universities in two countries: the University of Hasselt and Maastricht University.

UHASSELT
KNOWLEDGE IN ACTION

www.uhasselt.be
Universiteit Hasselt
Campus Hasselt:
Martelarenlaan 42 | 3500 Hasselt
Campus Diepenbeek:
Agoralaan Gebouw D | 3590 Diepenbeek

UHASSELT
KNOWLEDGE IN ACTION

Maastricht University

Faculty of Medicine and Life Sciences
School for Life Sciences
Master of Biomedical Sciences

Master's thesis

Conductive MXene-based bioink for integrating biomimetic electronics into new 3D skin model

Yana Heyvaert

Thesis presented in fulfillment of the requirements for the degree of Master of Biomedical Sciences, specialization Bioelectronics and Nanotechnology

SUPERVISOR :
Prof. dr. Anitha ETHIRAJAN

SUPERVISOR :
Prof. dr. Roman ANTONANZAS PEREZ

CO-SUPERVISOR :
Prof. Dr. Miguel Angel MATEOS TIMONEDA

MENTOR :
Dhr. Maximilian JERGITSCH

Conductive MXene-based bioink for integrating biomimetic electronics into new 3D skin model

Yana Heyvaert[1,2], Maximilian Jergitsch[2,3], Roman Antoñanzas Pérez[2,3], and Miguel Angel Mateos Timoneda[2,3]*

[1]Hasselt University, Campus Diepenbeek, Agoralaan Gebouw D – 3590 Diepenbeek, Belgium
[2]Bioengineering Institute of Technology, Universitat Internacional de Catalunya, Josep Trueta – 08195 Sant Cugat del Vallès, Barcelona, Spain
[3]Department of Basic Sciences, Faculty of Medicine and Health Science, Universitat Internacional de Catalunya, Josep Trueta – 08195 Sant Cugat del Vallès, Barcelona, Spain

*Running title: *Conductive bioink for integrating electronics*

To whom correspondence should be addressed: Miguel Angel Mateos Timoneda, Tel: +34 935 042 000; Email: mamateos@uic.es

Keywords: conductive bioink, 3D bioprinting, MXene, skin tissue engineering

ABSTRACT

Bioprinting of skin tissue has recently gained significant interest as an alternative approach for treating injuries and facilitating transplantation. However, the inability to monitor and control the internal evolution of the engineered tissue remains a challenge. Integrating skin tissue with flexible electronics offers a novel platform for continuously monitoring and modulating skin activity, laying the foundation for intelligent tissues that could offer breakthroughs in tissue engineering and healthcare. To establish a fully functional hybrid platform with sensing and tuning abilities, it is essential to render the engineered tissue conductive. MXenes have emerged as highly conductive, versatile, and biocompatible compounds with various applications in biomedicine. In this study, conductive bioinks were developed with various concentrations (0.5, 1, and 2% (w/v)) of MXene in a multicomponent hydrogel containing alginate, gelatine, and methyl cellulose. Rheological measurements showed little differences in viscoelastic properties for lower concentrations of MXene, resulting in bioinks that show similar printability. Printed structures presented good structural integrity, without severe collapse. Moreover, the presence of 1% (w/v) MXene improved strand definition. However, a high concentration of MXene negatively impacted both viscoelastic and printing properties. MXene enhanced conductivity within the samples, which increased with concentration. Cell viability tests did not show immediate cytotoxic responses, proving the biocompatible nature of the nanomaterial. This work demonstrates that incorporating MXene can create a conductive bioink for skin tissue engineering, without compromising printability and cell survival.

GRAPHICAL ABSTRACT

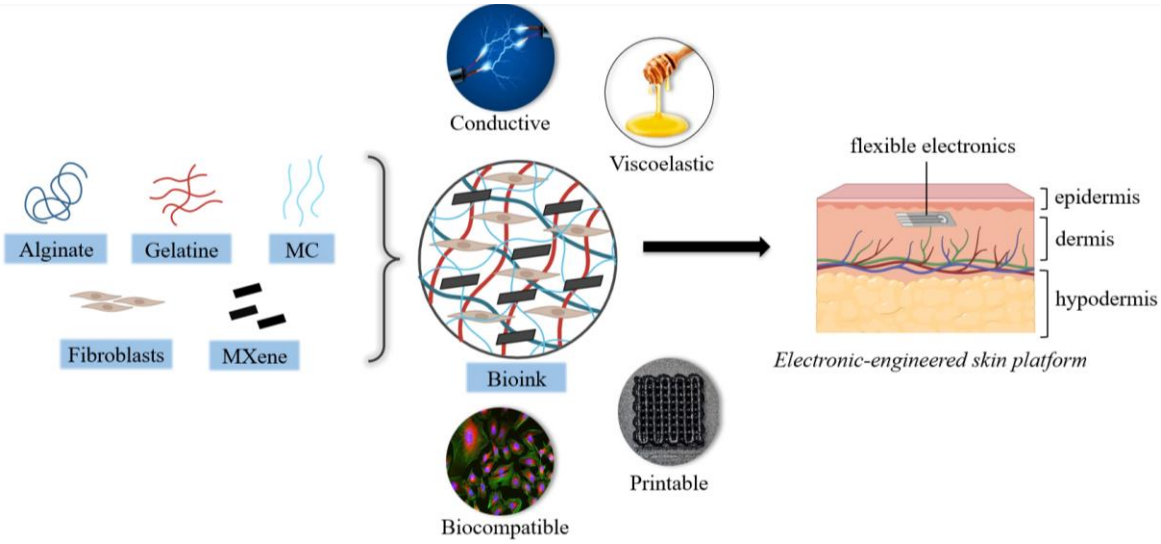

INTRODUCTION

The skin is the largest organ of the human body and acts as the first line of defence from the external environment. Severe damage from the skin greatly impairs its functions (1). Autografts and allografts remain the standard treatments for wound healing but are scarce due to the lack of viable transplantable skin as well as expected immune responses and potential disease infection (2-4). Additionally, there is a global demand for more representative models in drug development (5). The current processes mostly involve costly and time-consuming *in vivo* animal testing and *in vitro* cell cultures to evaluate the toxicity and efficacy of various compounds and their derivatives (6). Animal models remain the golden standard for preclinical evaluations. However, it is argued that they do not adequately represent effects in humans, are difficult to analyse, and bring about ethical questions (7, 8). *In vitro* cell cultures, on the other hand, are often too simplistic, and thus, do not reflect metabolic effects on non-targeted tissue due to the lack of tissue-tissue and tissue-organ communication (9, 10).

3D bioprinting has emerged as a revolutionary technology in the field of tissue engineering, offering the potential to create functional and personalised tissue constructs for various applications (11-13). In extrusion-based bioprinting, specifically, bioinks are extruded from a nozzle and precisely deposited as filaments in a layer-by-layer manner (14). A bioink is defined as a solution of biomaterials, usually hydrogels, that encapsulates cells and other biologically active compounds (15). It plays a crucial role in creating self-sufficient, functional tissue by providing a supporting microenvironment for the printed cells. Therefore, the scaffold must exhibit high biocompatibility and biodegradability, along with increased cell adhesion, proliferation, and differentiation (16, 17). Moreover, the mechanical stability of the bioink is of great importance. The bioink must present a viscosity low enough to facilitate extrusion from the 3D printer without subjecting laden cells to high shear stress, yet high enough to sustain their predefined 3D structure after printing (18-20). Hydrogels composed of natural biomaterials like alginate, an algae-derived polymer, and gelatine, a derivative of collagen, are widely applied in the bioprinting of skin tissue due to their biocompatibility, cell adhesion, and shear-thinning properties (21-23). The latter implies that the materials' viscosity decreases with increasing shear rate, thus exhibiting so-called viscoelastic behaviour (24). This property can be studied through rheology, which provides information on the storage modulus (G') and the loss modulus (G''). These parameters describe the solid-like behaviour (G') and the liquid-like behaviour (G'') of the hydrogel, or the elasticity and viscosity, respectively. The ratio of these two variables is defined as the loss tangent (G''/G'), or tanδ, and is often employed as an indicator of the printability of the material (25, 26). Alginate hydrogels present more viscosity than elasticity (G' < G''), while the opposite is true for gelatine-only hydrogels. The combination of these compounds presents a synergistic effect of these parameters, creating a bioink formula suitable for bioprinting skin tissue (26, 27).

When encapsulating cells into biomaterials, however, all other biological microorganisms must be destroyed through a sterilisation process. Autoclavation is a fast and effective sterilisation technique, although it is known to alter the molecular structures of both alginate and gelatine (28, 29). This results in decreased viscosity and mechanical stability, thereby reducing the printability of these inks (Figure S1) (30, 31). Methyl cellulose has been applied previously as a thickening additive for alginate-based inks to improve their viscosity (32, 33). Jergitsch et al. have conducted an extensive study on the combined effects of methyl cellulose, sucrose, and salt on the properties of the bioink (34). It was shown that high concentrations of salt and sucrose increased the elastic portion (G') of the viscoelastic parameters, consequently reducing tanδ and improving the shape fidelity of the bioinks. When combined with moderate concentrations of methyl cellulose, this resulted in enhanced printability and cell survival. Thus, this multicomponent hydrogel formulation shows great potential for bioprinting skin tissue.

Over the years, various skin substitutes have been developed. For example, products like Integra® and Dermagraf® are already commercialised for clinical treatment of burns and chronic wounds (35, 36). Despite these advances in tissue engineering, the inability to monitor and control the internal evolution of tissue remains a challenge (37). Current research explores the development of flexible electronics with monitoring and actuating

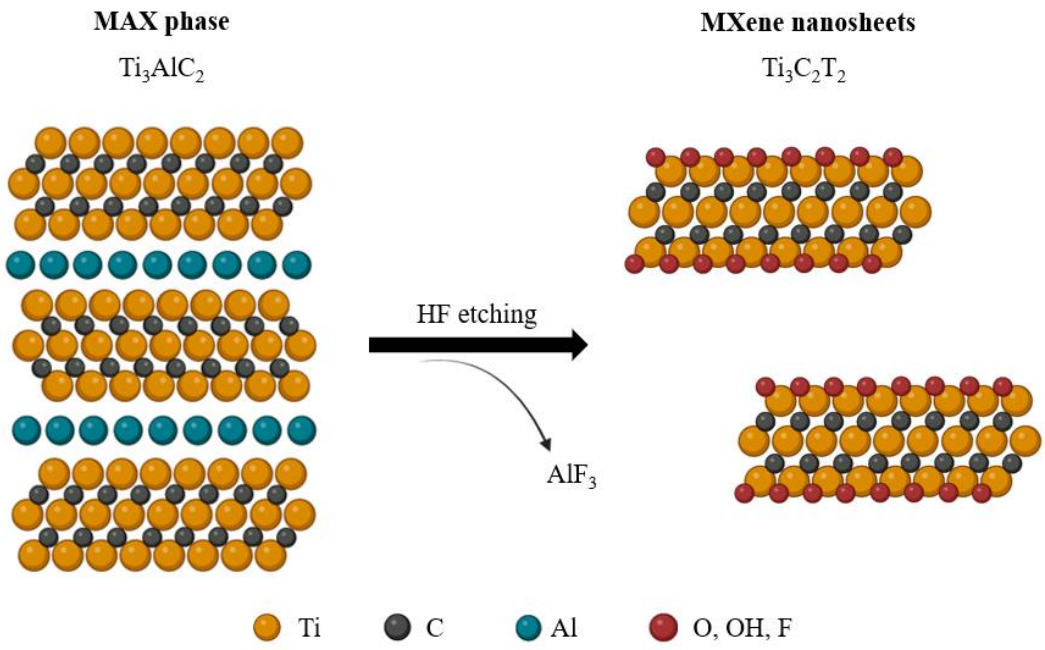

Fig. 1 – Synthesis of MXene ($Ti_3C_2T_2$) through hydrofluoric acid (HF) etching.

abilities. These biomimetic electronics are specifically designed to fit the complex dynamics and mechanical properties of native tissue (38, 39). Merging these electronics with tissue paves the way to continuous monitoring and actuation through drug delivery or electrical stimulation, which has great potential in tissue engineering, biomedicine, and bionics (40, 41). The risks of adverse effects caused by implanted devices can be greatly reduced since the electronic compound is fully integrated and compliant with the natural environment (42, 43). This will also achieve more qualitative data and reduce the need for invasive and expensive diagnostic testing (44, 45). Implementing these new electronics would further aid the diagnosis and ongoing treatment of patients with chronic diseases by enabling timely and remote interventions, thereby moving away from the current clinic-centred healthcare system (46, 47). Furthermore, a more comprehensive and personalised understanding of biological processes at the cellular and molecular level in various tissue models would be facilitated, which subsequently benefits drug- and cosmetic development (48, 49). Finally, integrated electronics can enhance the functionality of prosthetics, allowing for increased natural movement and sensory feedback (50).

In order to seamlessly integrate electronic compounds and establish a fully functional hybrid platform, the bioink needs to be conductive. However, most cell-laden bioinks are composed of hydrogels, which are electrically insulating matrices. This issue can be resolved by incorporating conductive nanomaterials like metal nanoparticles and carbon-based materials (18). Various studies have shown that the incorporation of these compounds results in bioinks that bring forth enhanced properties, such as increased conductivity, improved mechanical stability, better shape fidelity, and augmented cell viability and proliferation (51-54). However, using these compounds creates several difficulties. Nanoparticles are prone to aggregation in aqueous media and tend to form inhomogeneous mixtures (55). Carbon materials like carbon nanotubes and graphene are difficult to disperse in aqueous solutions due to their inherent hydrophobicity. This issue can be addressed by modifying graphene into graphene oxide or reduced graphene, although this compromises mechanical and electrical properties (56, 57).

A new family of 2D materials, called MXenes, was discovered by Gogotsi and colleagues in 2011 (58). These materials comprise a wide array of metal carbides, nitrides, and carbonitrides, most often prepared through chemical etching of their corresponding MAX phase (Figure 1). This precursor is

represented by the general denotation $M_{n+1}AX_n$, where M indicates an early transition metal (e.g., Ti, Cr, Nb, V, Sc, or Mo), X refers to carbon and/or nitrogen, and A typically involves a group 13 or 14 element of the periodic table, such as Al, Si, and Ga (59). Selective etching is facilitated by the bonding character of the M-A bond, which is purely metallic and thus weaker than the M-X bond that also possesses covalent bonding properties. Eliminating this A-layer gives rise to other surface termination groups T_x (e.g. O, OH, F), forming a new layered material represented by the general formula $M_{n+1}X_nT_x$ (60).

MXenes have attracted great interest in a variety of advanced technologies due to their versatile characteristics. Their exceptional crystal structures, hydrophilic surface chemistries, high electrical conductivities, and excellent thermal and mechanical properties have led to applications in energy storage (61), electronics (62), electrocatalysts (63), and lithium-ion batteries (64), to name a few. These materials have sparked interest in biomedical applications as well due to the extensive opportunities for functionalisation of their end groups and their biocompatible nature (65). This has led to advances in drug delivery (66), biosensing (67), and photothermal and photodynamic therapy (68, 69). Additionally, several studies have reported the incorporation of these metal nanomaterials into bioinks for tissue engineering applications. Research has shown that MXenes enhance conductivity within hydrogel matrices and improve the printability and stability of the material (70, 71). Moreover, MXenes appear to be non-cytotoxic and even enhance cell growth in both cardiomyocytes (72) and human mesenchymal stem cells (73). It is evident that this novel material poses an excellent candidate for developing a bioink with suitable properties.

In this study, a conductive bioink was developed for integrating biomimetic electronics into a new 3D skin model. Conductivity was established by incorporating various concentrations of MXene ($Ti_3C_2T_2$) into a multicomponent hydrogel formulation containing alginate, gelatine, methyl cellulose, sucrose, and salt. The mechanical properties of the bioinks were evaluated and the printability was assessed. Furthermore, human fibroblasts were encapsulated into the material to analyse the biocompatibility. The present work addresses the research question regarding the potential of this 2D nanomaterial to establish electrical conductivity within a bioink while preserving structural integrity post-printing and ensuring cell survival. It was hypothesised that MXene enhances conductivity within the hydrogel matrix, improves the mechanical properties of the bioink, and promotes cell viability.

EXPERIMENTAL PROCEDURES

Chemicals – Ti_3AlC_3 (MAX; 910767), gelatine from porcine skin (G1890), methyl cellulose (M0512), phosphate-buffered saline (PBS; P4417), and sucrose (P4417) were purchased from Sigma Aldrich. Hydrofluoric acid 40% (HF; 213070) and sodium alginate (A3249) were obtained from PanReac AppliChem. Dulbecco's Modified Eagle's Medium (DMEM; 81212231) was acquired from ATCC.

Synthesis of MXene compound – MXene ($Ti_3C_2T_2$) was synthesised through HF etching of the MAX-precursor Ti_3AlC_3, as previously described (74). In short, 2 g of Ti_3AlC_3 was dissolved in 15 mL of MilliQ water. Next, 25 mL of HF was added gradually while stirring at room temperature. Once the whole volume of acid was added, the recipient was covered and the mixture was left to react for 5 hours. After this time, the product underwent multiple rounds of centrifugation (4000 rpm, 5 minutes) in deionised water until the supernatant reached pH 6. The compound was then washed once in 70% ethanol and incubated afterwards at 37°C until dry.

Preparation of hydrogel formulations – A base stock solution of 2% (w/v) sodium alginate and 1% (w/v) gelatine was prepared. First, 10% (w/v) sucrose was dissolved in 100 mL PBS 3X (3g/100mL) at 40°C. Next, 1% (w/v) gelatine was added and the solution was mixed for approximately 1 hour. After the gelatine was properly dissolved, the heat was turned off and 2% (w/v) alginate was added. This solution was stirred carefully for 2 hours until a homogeneous mixture was obtained. After this, the stock solution was sterilised by autoclavation at 120°C for 15 minutes. Meanwhile, the appropriate amounts of methyl cellulose (6% w/v) and MXene (0.5%, 1%, and 2% w/v) were weighed together in plastic Speedmixer cups and were autoclaved as well. After sterilization, 10 mL of hot (65-70°C)

alginate-gelatine mixture was added to the powders using a high-viscosity liquid pipet tip, while working in aseptic conditions. All components were then mixed in a Speedmixer DAC 150.1 FVZ (FlackTek, Inc.) at 700 rpm for at least 5 minutes. After this, the homogeneous mixture was transferred to 5 mL syringes, which were stored overnight at 4°C to allow complete gelation. The samples were named after their MXene concentration, as represented in Table 1.

Table 1 – Composition of hydrogel formulations.

Abbreviation	%w/v MXene
MX0	0
MX0.5	0.5
MX1	1
MX2	2

Rheological measurements – Rheometric characterization was conducted employing a TA Instruments Discovery Hybrid Rheometer-2 equipped with a Peltier plate for temperature control. All experiments were executed at 25°C, using a 20 mm stainless steel upper plate and a measuring gap of 0.5 mm. An amplitude sweep was performed with a strain range from 0.01 to 500% at a constant oscillating frequency of 10 rad/s. To evaluate the crosslinking kinetics of the bioink formulations, oscillatory measurements were conducted at a constant angular frequency of 10 rad/s and 1% strain. Samples were equilibrated for 60 seconds before adding 0.15 M $CaCl_2$. The crosslinking process was then monitored for 10 minutes. The viscosity and shear thinning behaviour were assessed through rotational measurements with increasing shear rate from 0.01 to 100 s^{-1}.

3D (bio)printing – Various 3D constructs were printed employing a custom-modified bioprinter equipped with a syringe pump extruder print head (Figure S2). G-codes for the different designs were generated using a cutsom Phyton script. The bioinks were extruded using a 22G needle (Nordson EFD SmoothFlow Tapered Tips) at room temperature, with the printing bed temperature configured to 40°C.

Printability and structural integrity – The structural integrity of the formulations was evaluated by printing 6-layer (layer height: 450 µm) cubical structures, without infill. Photographic images were taken with a custom-made camera tripod at a fixed distance and angle. The structural integrity of the different bioink formulations was quantified by comparing the height among the samples at 20 different points employing ImageJ software (75). A showcase construct of MX1 was printed in an upright square lattice design without perimeter, containing 12 layers (layer height: 340 µm) and 9 strands per layer (spacing: 1.8 mm).

Strand morphology – 3-layered cubical structures (layer height: 450 µm) with 7 strands per layer (spacing: 1.8 mm) were printed in sterile conditions using an upright square lattice design without perimeter. After printing, the structures were crosslinked with 0.15 M $CaCl_2$ for 5 minutes. Mosaic confocal images (Leica SP8) of the samples were taken immediately after printing and crosslinking, and at different time points (day 1, day 4, day 7, day 14) after incubation in DMEM. The strand width of the middle layer was measured at 20 different points employing ImageJ software.

Electrochemical characterization – Conductivity measurements were conducted by a simple set-up using a potentiostat (Autolab PGSTAT302N). Scaffolds were printed in an upright square lattice design without perimeter, containing 4 layers (layer height: 340 µm) with 5 strands per layer (spacing: 1.7 mm). After printing, the structures were crosslinked with 0.15 M $CaCl_2$ for 5 minutes, after which they were stored in a buffer containing 0.15 M NaCl and 0.01 M $CaCl_2$. All samples were dried for 2 hours before measuring. Meanwhile, a sample cover was prepared by sticking two strips of copper tape parallel to each end of a piece of non-conductive plastic. The cover with the sample was then attached to two clamp electrodes, which were in turn connected to the potentiometer. The conductivity of the samples was evaluated by measuring the current generated by voltages between 0.5V and 2V, subsequently plotting current to voltage.

Cell culture conditions – Human foreskin fibroblasts (HFF-1) were purchased from ATCC. The cells were cultured in DMEM, enriched with 15% fetal bovine serum and 1% penicillin/streptomycin. The medium was changed every other day and the culture

environment was maintained at 37°C in a 5% CO_2 atmosphere. Cells were expanded after reaching 70-80% confluency, and all experiments were conducted using HFF-1 between passages 16 and 18.

Bioink preparation and scaffold design – HFF-1 cells were detached by incubation with Trypsin/EDTA and were resuspended in cell culture medium to reach a concentration of 10^6 cells/mL. Each hydrogel formulation was mixed carefully with cell suspension by passing back and forth between two 3 mL syringes using a screw-like luer lock syringe adapter (76). Scaffolds for biological characterisation were printed in sterile conditions using an upright square lattice design without perimeter, containing 4 layers (layer height: 340 µm) and 5 strands per layer (spacing: 1.7 mm).

Cell viability – Printed scaffolds containing HFF-1 were cultured in enriched cell medium for 7 days. Cell survival was assessed by calcein-AM/propidium iodide (pI) staining, according to the manufacturer's instructions. At different time points (days 1, 3, and 7), the scaffolds were incubated with staining solution for 20 minutes, followed by washing in $NaCl/CaCl_2$ (0.15 M/0.01M) buffer. Z-stack images (7 layers, 100 µm) were acquired by confocal fluorescence microscopy (Leica SP8).

Cell proliferation – Fibroblast proliferation in MX0 and MX0.5 was evaluated by a PicoGreen® assay. Cell-laden scaffolds were incubated in enriched cell medium for 14 days. The scaffolds were submerged in a cell lysis solution (0.1% Triton-100X in PBS) at various time points (day 1, 7, and 14) and stored at -80°C until analysis. The concentration of DNA was determined by mixing 100 µL of sample with 100 µL of PicoGreen reagent. The fluorescence intensity was measured at excitation and emission wavelengths of 485 nm and 535 nm, respectively, employing a multimode microplate reader (Tecan Infinite 200Pro). The amount of DNA was evaluated using a standard curve of DNA combined with cell-free scaffolds of MX0.

Statistical analysis – All measurements were collected in triplicates and expressed as mean ± standard deviation (SD) in OriginPro. The data was analysed by one-way ANOVA, followed by post-hoc Tukey testing. A *P*-value < 0.05 was considered significant for all analyses.

RESULTS AND DISCUSSION

Rheological characterisation – The mechanical properties of the bioink formulation are crucial for ensuring shape fidelity and protecting the laden cells during printing. Rheological measurements provide valuable insights into the ink's behaviour throughout the printing process. An amplitude sweep quantifies the storage modulus (G'), loss modulus (G"), and loss tangent ($\tan\delta = G"/G'$), thereby describing the viscoelastic behaviour. Here, all formulations are dominated by G' until it intersects with G" (Figure S3). The zone preceding this intersection defines the linear viscoelastic region (LVER), where a linear dependence exists between moduli/tanδ and applied strain or stress (77).

By comparing the moduli of the different bioink conditions within this linear window (Figure 2A), no difference was observed between MX0 and MX1. However, the moduli of the formulations MX0.5 and MX2 were significantly reduced. This effect was most profound in MX2. As a result, the tanδ of this formulation increased notably (Figure 2B). According to literature, lower tangent values are often associated with improved printability and structural stability (26, 34, 78). Hence, inferior printing properties could be expected for MX2, while the other formulations should present similar characteristics. The enhancement of rheological parameters with increasing MXene concentration can be attributed to augmented interparticle interactions between the 2D nanosheets (79) and elevated molecular interactions between the carbide functional groups and the polymer backbones (80, 81). However, it is not clear why 2% w/v MXene suddenly breaks the trend and induces the opposite effect in this hydrogel formulation. One explanation could be the agglomeration of the MXene flakes. Although MXene is inherently hydrophilic and stable in aqueous dispersion, high salt concentrations could influence their tendency to aggregate (82).

Printable materials ideally exhibit shear-thinning behaviour, which allows the material to flow as a result of decreasing viscosity when shear stress is applied. Increased shear-thinning behaviour has been shown to lower the extrusion pressure, thereby lowering the stress exerted on embedded cells (19). Here, all

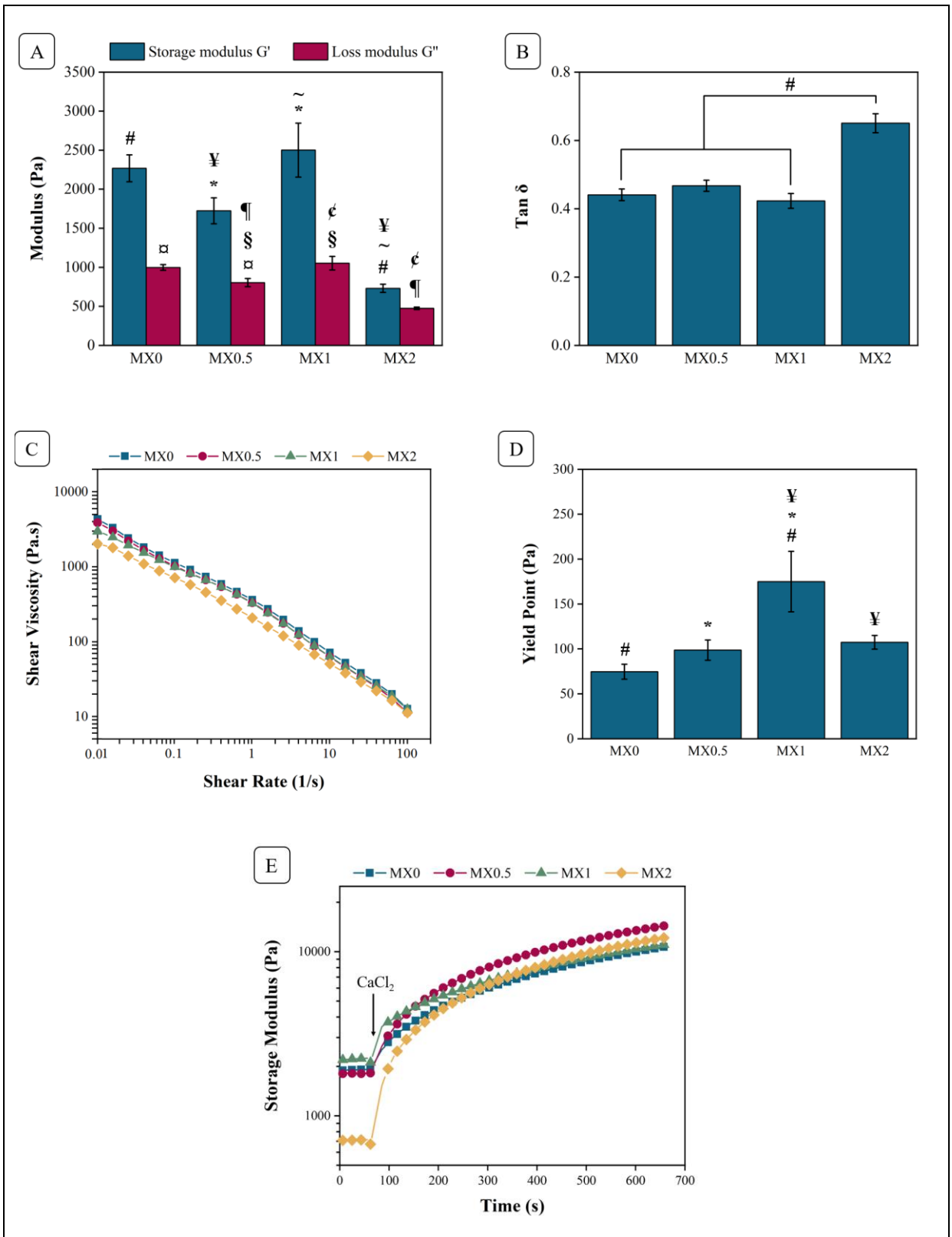

Fig. 2 – Rheological characterization**.** A) Comparison of moduli among different conditions at 0.1% oscillation strain. B) Comparison of loss tangents at 0.1% oscillation strain. C) Shear thinning behaviour of various conditions. D) Yield points. E) Evolution of storage moduli during crosslinking with 0.15 M $CaCl_2$.
Legend: ¤: $P < 0.05$; *, ¥, §: $P < 0.01$; ¶: $P < 0.001$; #, ~, ¢: $P < 0.0001$.

formulations exhibited shear-thinning behaviour (Figure 2C). Previous research has reported that the incorporation of MXene elevates shear thinning properties in hydrogels (83, 84). In this case, however, there was no profound difference observed between the conditions. At a shear rate of 100 s^{-1}, the formulations showed similar shear viscosities of 12.48 ± 0.76, 11.04 ± 0.98, 12.31 ± 0.86, and 11.00 ± 0.82 Pa.s for MX0, MX0.5, MX1, and MX2, respectively. Thus, it can be stated that MXene did not negatively impact the shear-thinning behaviour of the multicomponent hydrogel.

The yield point of materials is a property signifying the stress required to transition from elastic behaviour to plastic deformation (77). In other words, it is the point at which the material starts to flow. Figure 2D shows a significantly increased yield point for MX1, while no notable difference was observed between MX0, MX0.5, and MX2. This implies that greater extrusion pressure is necessary to extrude the MX1 bioink. While this is expected to yield positive results in extrudability and shape fidelity, it could negatively impact cell survival (85).

Alginate-based gels are most often stabilized by ionic crosslinking of their carboxyl end groups with Ca^{2+}-ions. However, it is known that the rheological properties change with crosslinking density (86, 87). The results in Figure 2E depict the evolution in storage moduli during crosslinking with 0.15 M $CaCl_2$. The storage modulus for MX0.5 and MX2 appears to increase more rapidly during crosslinking, given the steepness of the slopes. Although MX2 initially exhibited significantly lower G', crosslinking enabled recovery of the material to a strength comparable to that of the other formulations. It can be concluded that MXene did not affect the crosslinking kinetics.

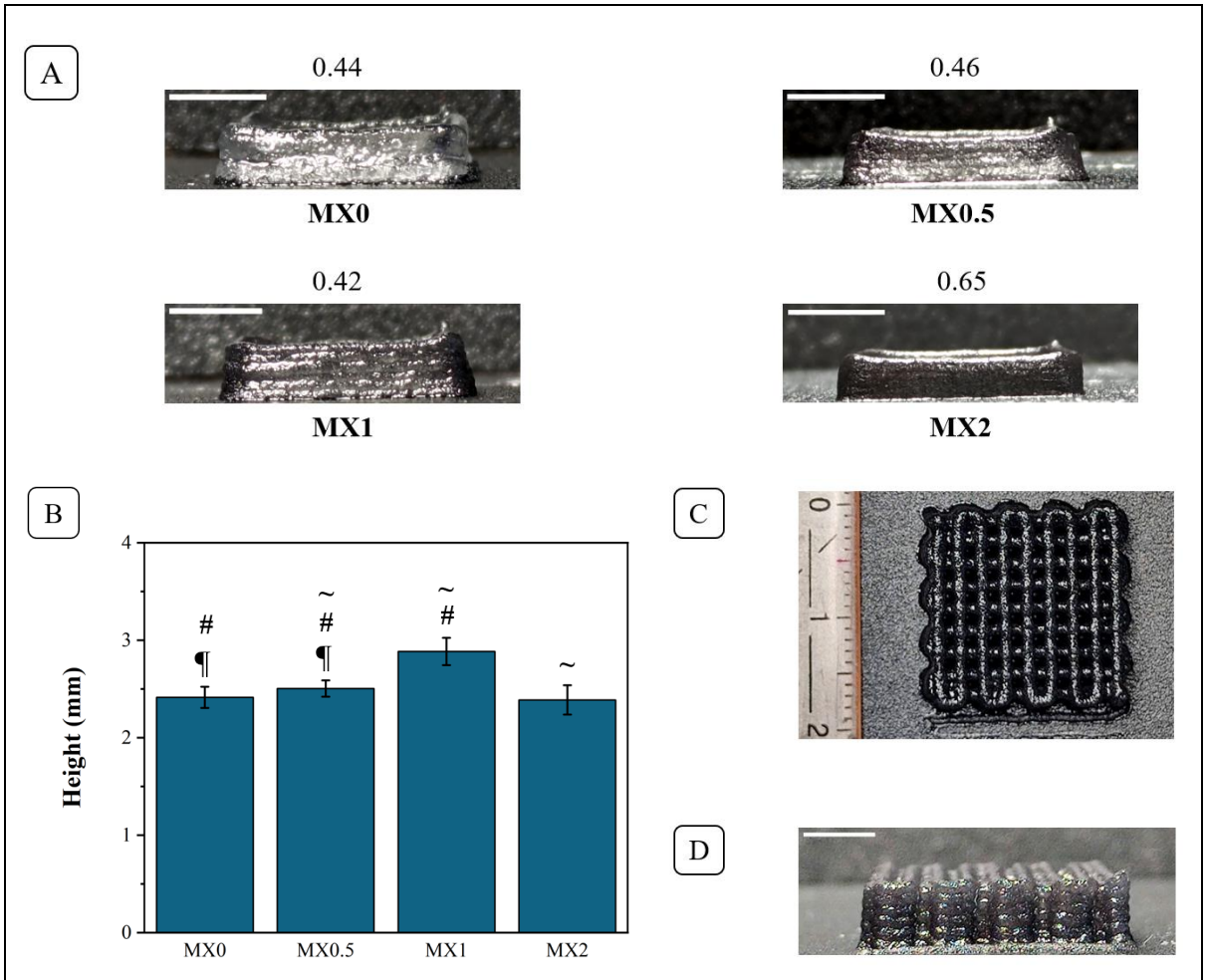

Fig. 3 – Evaluation of the structural integrity**.** A) 6-layer cubical structures with different loss tangent values. Scale bar: 5 mm. B) Comparison of structural height among the samples. Legend: ¶: $P < 0.001$; #, ~: $P < 0.0001$. Showcase MX1 C) top view, and D) side view. Scale bar: 5 mm.

Printability and structural integrity – The structural integrity is an indication of how well the bioink can hold its predetermined structure. The shape fidelity of the bioink formulations was evaluated by printing a construct composed solely of a 6-layered perimeter and comparing the height of the structures among the test groups. Figure 3A shows the side profile of the printed samples. The samples show a tendency to collapse inward, although no severe collapse occurred. The individual filaments are extremely profound in MX1, while they seem to disappear in the other constructs.

Figure 3B compares the different heights of the printed samples. The relationship between tanδ and shape fidelity described earlier is reflected here. The samples with lower loss tangent, namely MX0 and MX1, present higher average heights compared to the other conditions. Studies have shown that a higher tanδ results in loss of shape fidelity (34), as was observed here in MX2. This sample presented significantly smaller heights compared to the other constructs.

A large construct of sample MX1 is shown in Figures 3C and 3D. The excellent printability predicted by its rheological characterization is evident here. With a low loss tangent and high yield point, this formulation could print large constructs with improved strand definition and

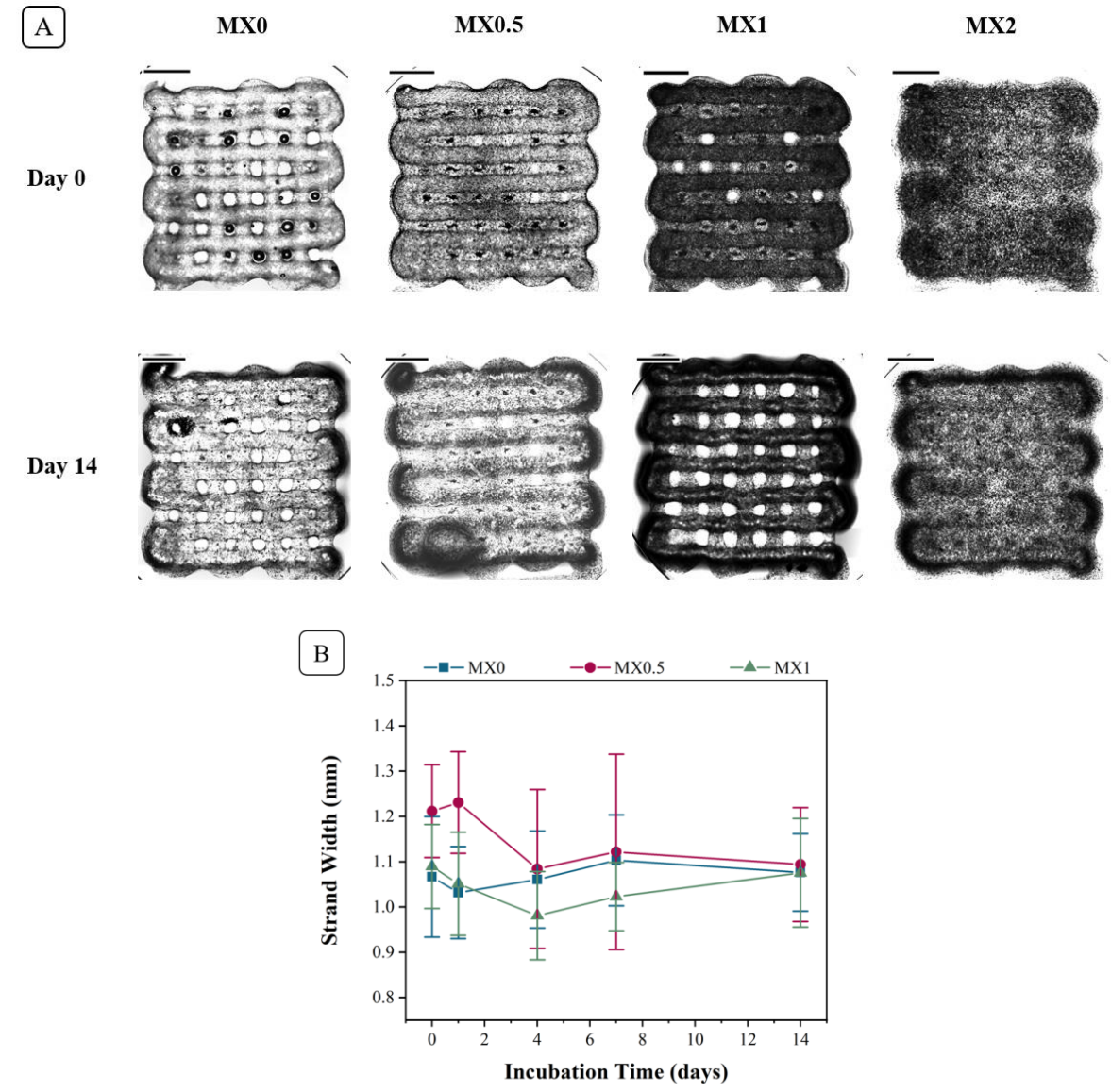

Fig. 4 – Strand width morphology. A) Confocal images of printed samples at different stages. Scale bar: 3 mm. B) Strand width change at different time points after incubation in DMEM.

maintained its structure without any sign of collapse. A concentration of 1% w/v MXene evidently improved shape fidelity in the hydrogel formulation.

Strand morphology – The strand width of printed scaffolds was monitored during 14 days of incubation in DMEM. Figure 4A illustrates the samples at different time points. MX2 was not considered in this analysis because the individual strands were too difficult to distinguish. This can be considered a direct representation of the previous results: the increased loss tangent correlates to diminished shape retention. By day 14, the spaces between the filaments were more visible. Figure 4B shows the change in strand width of the remaining conditions. There was no significant difference observed among the conditions. It is important to note that, although it is known that methyl cellulose diffuses out over time (33, 88), MXene has remained within the scaffolds. This is crucial in order to collect and propagate data when incorporating electronics in further applications.

Electrical characterisation – The conductivity of printed scaffolds was evaluated for all conditions using a custom set-up employing a potentiometer (Figure 5A). An electrical circuit was established by constructing two electrodes from copper tape on a piece of non-conductive plastic, and introducing a sample as the resistance that closes the circuit between the two copper electrodes. The scaffolds contain PBS-buffer and were stored in NaCl/$CaCl_2$-buffer to keep them stabilized over time. It is well known that buffer solutions present some level of conductivity due to the ions in solution, as first described by Debye and Hückel (89, 90). Therefore, the samples were dried for 2 hours before measuring so that interference by the charged ions was eliminated as much as possible. After this time, voltages between 0.5 to 2V were applied to the circuit and the corresponding current was recorded. As

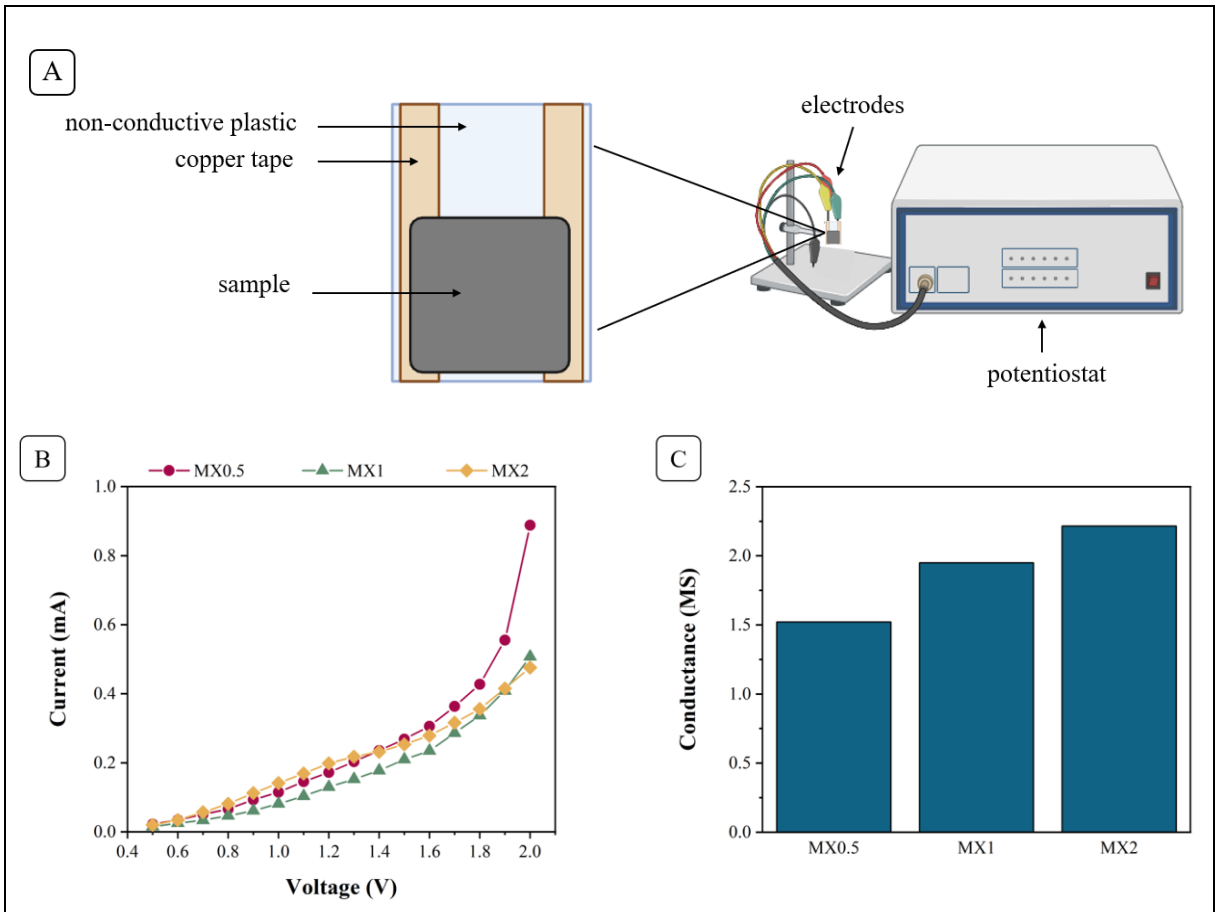

Fig. 5 – Electrical characterization. A) Set-up. B) I/V-curve of MX0.5, MX1, and MX2. C) Effect of MXene concentration on conductivity. MS: Mega Siemens (10^6 $\Omega^{-1}m^{-1}$).

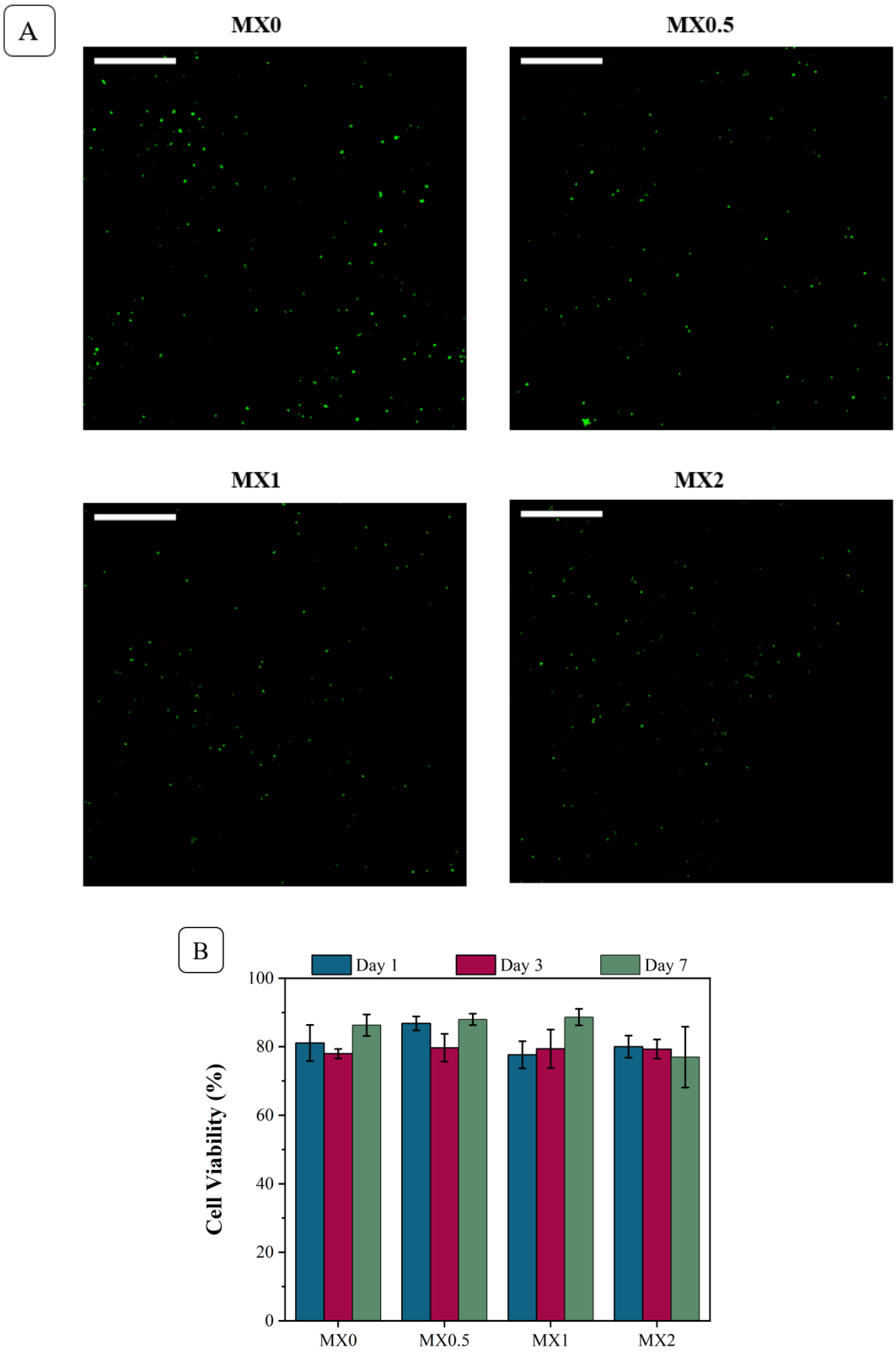

Fig. 6 – Effect of bioink samples on cell viability. A) Confocal microscopic images of HFF-1 containing MX0, MX0.5, MX1, and MX2 scaffolds on day 1 of incubation in enriched DMEM. Scale bar: 500 µm. B) Cell viability among the conditions at different time points.

depicted in Figure 5B, the samples presented a certain trend when current is plotted in function of voltage. No response was recorded for MX0, and the other formulations did not exhibit any current at voltages below 0.5V. Beyond this point, the current increases with rising voltage, although not precisely in a perfect linear fashion. In order to estimate the conductance, a linear relationship needs to be established. The most accurate linear correlation was found between 1V and 1.9V (Figure S4). After linear fitting and appropriate calculations, the conductance σ for MX1, MX0.5, and MX2 was estimated using the following equation (91):

$$\sigma = \frac{1}{\rho} = \frac{IL}{VA}$$

in which ρ represents the resistivity of the material, I and V are the current and the voltage, and L and A stand for the length and the area of the scaffold, respectively. Figure 5C shows the conductivities of the samples. The estimated conductance values were 1.52, 1.95, and 2.22 $MS.m^{-1}$ for MX0, MX1, and MX2, respectively. As expected, the conductance increased with MXene concentration. These findings proof that MXene was able to establish conductivity within the hydrogel matrix.

Cell viability – Biocompatibility of the different samples was evaluated in HFF-1-laden scaffolds. Human fibroblasts were selected for this study due to their abundance in the dermis layer of human skin (1, 2). Cytotoxicity can easily be tested by a live/dead assay. Here, a staining solution containing calcein-AM and propidium iodide was used to distinguish live from dead cells. In living cells, enzymes called esterases convert calcein-AM to calcein, a green fluorescent compound. On the other hand, dead cells do not present esterase activity but possess a damaged plasma membrane. This allows penetration of propidium iodide to bind the cell's DNA, creating a red fluorescence (92). After incubation, the fibroblasts were visualised using fluorescence microscopy and the cell viability was determined.

Green fluorescence was predominant in all conditions (Figure 6A). Figure 6B compares the cell viability between the different conditions at different time points. Viabilities greater than 75% were observed for all conditions. Furthermore, no significant differences were observed among the samples, indicating that the bioink sufficiently shielded the cells during printing. Moreover, the elevated yield stress found in MX1 did not hinder cell survival during printing. These findings confirm the previously reported biocompatibility of MXene (65, 72, 93).

Cell proliferation – Cell growth was quantified by assessing the DNA content of HFF-1 using a PicoGreen assay. PicoGreen is a fluorochrome that selectively binds to double-stranded DNA in cells (94). A standard curve was prepared from stock DNA and incorporated cell-free printed MX0 scaffolds. These scaffolds were added to ensure identical conditions for generating qualitative results. Cell proliferation was evaluated in MX0 and

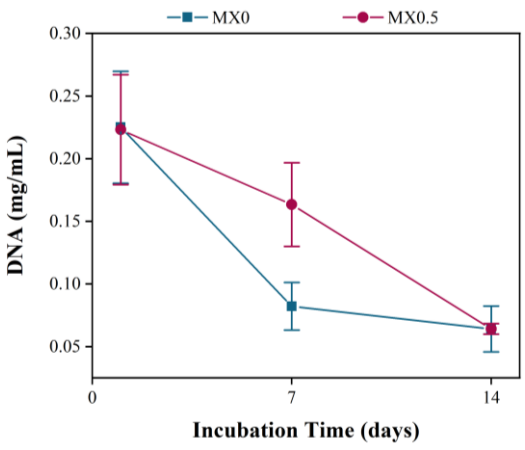

Fig. 7 – DNA content in MX0 and MX0.5 scaffolds at days 1, 7, and 14 of incubation in enriched DMEM.

MX0.5. The remaining conditions were not included due to complications. Nevertheless, analysis of two conditions can offer insight into whether this bioink formulation supports cell adhesion and facilitates cell proliferation.

Figure 7 shows the changes in DNA content over 14 days. The initial DNA concentrations were 0.225 ± 0.0447 mg/mL and 0.223 ± 0.0438 mg/mL for MX0 and MX0.5, respectively. At day 14, the values dropped to nearly one-fourth of the initial concentrations, implying that proliferation has not occurred.

For cells to interact with their environment, the scaffold must resemble the natural extracellular matrix (ECM). This means that the hydrogel matrix contains adhesion motifs to promote cell attachment (18, 95). Cell adhesion is important for cell migration, differentiation, and mechanotransduction, which ultimately lead to cell growth. Neither alginate nor methyl cellulose present good cell attachment properties, unless functionalised (11, 96). Gelatine, on the other hand, contains RGB-sequences (Arg-Gly-Asp) that allow for integrin binding by cells (97). However, these structures are probably destroyed in the current formulation during the sterilisation process, as mentioned before (28). Therefore, the high concentration of averting compounds combined with altered chemical structures is likely the cause of hindered proliferation in MX0 and MX0.5 scaffolds.

CONCLUSION AND FUTURE OUTLOOK

In this work, conductive multicomponent bioinks incorporating MXene were developed. Concentrations of 0.5% (MX0.5), 1% (MX1), and 2% (MX2) w/v MXene could easily be integrated into the hydrogel matrix consisting of alginate, gelatine, methyl cellulose, sucrose, and salt. The viscoelastic properties of MX1 bioink improved significantly, resulting in enhanced structural integrity and strand definition. The incorporation of MXene established conductivity within the matrix and increased with MXene concentration. All bioink formulations showed excellent cell viability (> 75%) when encapsulated with HFF-1, representing biocompatibility of the MXene nanosheets. However, cell proliferation was not observed within the control formulation MX0 and sample MX0.5, most likely due to the lack of adhesion sites in the matrix. Nevertheless, this study has successfully developed a conductive, printable bioink for potential in embedding biomimetic electronics into engineered tissue.

Future research should focus on establishing adherend sites within the matrix to allow proliferation of embedded cells and create a self-supporting skin layer. This could be achieved by functionalisation of hydrogel compounds or MXene, although sterilisation effects need to be considered. Additionally, it would be interesting to evaluate the microstructure within the bioink and investigate how porosity affect proliferation. Furthermore, the effect of electrostimulation on cell-laden scaffolds should be assessed. In future applications, both the scaffold and the embedded cells could be subjected to constant electrical cues. Therefore, it is important to investigate the effects on the stability of the scaffold as well as cell viability and proliferation.

REFERENCES

1. Tottoli EM, Dorati R, Genta I, Chiesa E, Pisani S, Conti B. Skin Wound Healing Process and New Emerging Technologies for Skin Wound Care and Regeneration. Pharmaceutics. 2020;12(8).
2. Tanfani JD, Monpara JD, Jonnalagadda S. 3D Bioprinting and Its Role in a Wound Healing Renaissance. Advanced Materials Technologies. 2023;8(17):2300411.
3. Kang MS, Jang J, Jo HJ, Kim WH, Kim B, Chun HJ, et al. Advances and Innovations of 3D Bioprinting Skin. Biomolecules. 2022;13(1).
4. Fishman JA, Greenwald MA, Grossi PA. Transmission of Infection With Human Allografts: Essential Considerations in Donor Screening. Clinical Infectious Diseases. 2012;55(5):720-7.
5. Sarkiri M, Fox SC, Fratila-Apachitei LE, Zadpoor AA. Bioengineered Skin Intended for Skin Disease Modeling. International Journal of Molecular Sciences. 2019;20(6):1407.
6. Khalil AS, Jaenisch R, Mooney DJ. Engineered tissues and strategies to overcome challenges in drug development. Adv Drug Deliv Rev. 2020;158:116-39.
7. Van Norman GA. Limitations of Animal Studies for Predicting Toxicity in Clinical Trials: Is it Time to Rethink Our Current Approach? JACC: Basic to Translational Science. 2019;4(7):845-54.
8. Sántha M. Biologia futura: animal testing in drug development—the past, the present and the future. Biologia Futura. 2020;71(4):443-52.
9. Esch MB, Smith AST, Prot J-M, Oleaga C, Hickman JJ, Shuler ML. How multi-organ microdevices can help foster drug development. Advanced Drug Delivery Reviews. 2014;69-70:158-69.
10. Kapałczyńska M, Kolenda T, Przybyła W, Zajączkowska M, Teresiak A, Filas V, et al. 2D and 3D cell cultures - a comparison of different types of cancer cell cultures. Arch Med Sci. 2018;14(4):910-9.
11. Olejnik A, Semba JA, Kulpa A, Dańczak-Pazdrowska A, Rybka JD, Gornowicz-Porowska J. 3D Bioprinting in Skin Related Research: Recent Achievements and Application Perspectives. ACS Synthetic Biology. 2022;11(1):26-38.
12. Papaioannou TG, Manolesou D, Dimakakos E, Tsoucalas G, Vavuranakis M, Tousoulis D. 3D Bioprinting Methods and Techniques: Applications on Artificial Blood Vessel Fabrication. Acta Cardiol Sin. 2019;35(3):284-9.
13. Yazdanpanah Z, Johnston JD, Cooper DML, Chen X. 3D Bioprinted Scaffolds for Bone Tissue Engineering: State-Of-The-Art and Emerging Technologies. Frontiers in Bioengineering and Biotechnology. 2022;10.
14. Zhang YS, Haghiashtiani G, Hübscher T, Kelly DJ, Lee JM, Lutolf M, et al. 3D extrusion bioprinting. Nature Reviews Methods Primers. 2021;1(1):75.
15. Gungor-Ozkerim PS, Inci I, Zhang YS, Khademhosseini A, Dokmeci MR. Bioinks for 3D bioprinting: an overview. Biomater Sci. 2018;6(5):915-46.
16. Deo KA, Singh KA, Peak CW, Alge DL, Gaharwar AK. Bioprinting 101: Design, Fabrication, and Evaluation of Cell-Laden 3D Bioprinted Scaffolds. Tissue Engineering Part A. 2020;26(5-6):318-38.
17. Murphy SV, Atala A. 3D bioprinting of tissues and organs. Nature Biotechnology. 2014;32(8):773-85.
18. Heinrich MA, Liu W, Jimenez A, Yang J, Akpek A, Liu X, et al. 3D Bioprinting: from Benches to Translational Applications. Small. 2019;15(23):1805510.

19. Matai I, Kaur G, Seyedsalehi A, McClinton A, Laurencin CT. Progress in 3D bioprinting technology for tissue/organ regenerative engineering. Biomaterials. 2020;226:119536.
20. Dvir T, Timko BP, Kohane DS, Langer R. Nanotechnological strategies for engineering complex tissues. Nature Nanotechnology. 2011;6(1):13-22.
21. Fayyazbakhsh F, Khayat MJ, Leu MC. 3D-Printed Gelatin-Alginate Hydrogel Dressings for Burn Wound Healing: A Comprehensive Study. IJB. 2022;8(4).
22. Pourchet LJ, Thepot A, Albouy M, Courtial EJ, Boher A, Blum LJ, et al. Human Skin 3D Bioprinting Using Scaffold-Free Approach. Advanced Healthcare Materials. 2017;6(4):1601101.
23. Liu J, Zhou Z, Zhang M, Song F, Feng C, Liu H. Simple and robust 3D bioprinting of full-thickness human skin tissue. Bioengineered. 2022;13(4):10090-100.
24. Żołek-Tryznowska Z. 6 - Rheology of Printing Inks. In: Izdebska J, Thomas S, editors. Printing on Polymers: William Andrew Publishing; 2016. p. 87-99.
25. Ramli H, Zainal NFA, Hess M, Chan CH. Basic principle and good practices of rheology for polymers for teachers and beginners. Chemistry Teacher International. 2022;4(4):307-26.
26. Gao T, Gillispie GJ, Copus JS, Pr AK, Seol YJ, Atala A, et al. Optimization of gelatin-alginate composite bioink printability using rheological parameters: a systematic approach. Biofabrication. 2018;10(3):034106.
27. Liu P, Shen H, Zhi Y, Si J, Shi J, Guo L, et al. 3D bioprinting and in vitro study of bilayered membranous construct with human cells-laden alginate/gelatin composite hydrogels. Colloids and Surfaces B: Biointerfaces. 2019;181:1026-34.
28. Carranza T, Zalba-Balda M, Baraibar MJB, de la Caba K, Guerrero P. Effect of sterilization processes on alginate/gelatin inks for three-dimensional printing. Int J Bioprint. 2023;9(1):645.
29. Dai Z, Ronholm J, Tian Y, Sethi B, Cao X. Sterilization techniques for biodegradable scaffolds in tissue engineering applications. J Tissue Eng. 2016;7:2041731416648810.
30. Chansoria P, Narayanan LK, Wood M, Alvarado C, Lin A, Shirwaiker RA. Effects of Autoclaving, EtOH, and UV Sterilization on the Chemical, Mechanical, Printability, and Biocompatibility Characteristics of Alginate. ACS Biomaterials Science & Engineering. 2020;6(9):5191-201.
31. Zhang F, Scull G, Gluck JM, Brown AC, King MW. Effects of sterilization methods on gelatin methacryloyl hydrogel properties and macrophage gene expressionin vitro. Biomed Mater. 2022;18(1).
32. Schütz K, Placht A-M, Paul B, Brüggemeier S, Gelinsky M, Lode A. Three-dimensional plotting of a cell-laden alginate/methylcellulose blend: towards biofabrication of tissue engineering constructs with clinically relevant dimensions. Journal of Tissue Engineering and Regenerative Medicine. 2017;11(5):1574-87.
33. Reakasame S, Dranseikiene D, Schrüfer S, Zheng K, Schubert DW, Boccaccini AR. Development of alginate dialdehyde-gelatin based bioink with methylcellulose for improving printability. Materials Science and Engineering: C. 2021;128:112336.
34. Jergitsch M, Alluè-Mengual Z, Perez RA, Mateos-Timoneda MA. A systematic approach to improve printability and cell viability of methylcellulose-based bioinks. Int J Biol Macromol. 2023;253(Pt 7):127461.
35. Manita PG, Garcia-Orue I, Santos-Vizcaino E, Hernandez RM, Igartua M. 3D Bioprinting of Functional Skin Substitutes: From Current Achievements to Future Goals. Pharmaceuticals. 2021;14(4):362.
36. Chang DK, Louis MR, Gimenez A, Reece EM. The Basics of Integra Dermal Regeneration Template and its Expanding Clinical Applications. Semin Plast Surg. 2019;33(3):185-9.

37. Feiner R, Dvir T. Engineering Smart Hybrid Tissues with Built-In Electronics. iScience. 2020;23(2):100833.
38. Lubrano C, Matrone G, Forro C, Jahed Z, Offenhäusser A, Salleo A, et al. Towards biomimetic electronics that emulate cells. MRS Communications. 2020;10:1-15.
39. Feiner R, Dvir T. Tissue–electronics interfaces: from implantable devices to engineered tissues. Nature Reviews Materials. 2017;3(1):17076.
40. Baran D, Corzo D, Blazquez G. Flexible Electronics: Status, Challenges and Opportunities. Frontiers in Electronics. 2020;1.
41. Xu C, Solomon SA, Gao W. Artificial intelligence-powered electronic skin. Nature Machine Intelligence. 2023;5(12):1344-55.
42. Wang X, Feiner R, Luan H, Zhang Q, Zhao S, Zhang Y, et al. Three-dimensional electronic scaffolds for monitoring and regulation of multifunctional hybrid tissues. Extreme Mechanics Letters. 2020;35:100634.
43. Tian B, Liu J, Dvir T, Jin L, Tsui JH, Qing Q, et al. Macroporous nanowire nanoelectronic scaffolds for synthetic tissues. Nat Mater. 2012;11(11):986-94.
44. Chen S, Qi J, Fan S, Qiao Z, Yeo JC, Lim CT. Flexible Wearable Sensors for Cardiovascular Health Monitoring. Advanced Healthcare Materials. 2021;10(17):2100116.
45. Abu-Saude M, Morshed BI. Characterization of a Novel Polypyrrole (PPy) Conductive Polymer Coated Patterned Vertical CNT (pvCNT) Dry ECG Electrode. Chemosensors. 2018;6(3):27.
46. Patel S, Park H, Bonato P, Chan L, Rodgers M. A review of wearable sensors and systems with application in rehabilitation. Journal of NeuroEngineering and Rehabilitation. 2012;9(1):21.
47. Sunwoo S-H, Han SI, Joo H, Cha GD, Kim D, Choi SH, et al. Advances in Soft Bioelectronics for Brain Research and Clinical Neuroengineering. Matter. 2020;3(6):1923-47.
48. Yi N, Cui H, Zhang LG, Cheng H. Integration of biological systems with electronic-mechanical assemblies. Acta Biomater. 2019;95:91-111.
49. Shirzaei Sani E, Xu C, Wang C, Song Y, Min J, Tu J, et al. A stretchable wireless wearable bioelectronic system for multiplexed monitoring and combination treatment of infected chronic wounds. Science Advances. 2023;9(12):eadf7388.
50. Cheng M, Jiang L, Fan S, Yang B, Dai J, Liu H. Development of a Multisensory Underactuated Prosthetic Hand With Fully Integrated Electronics. 2023;28:1187-98.
51. Zhu K, Shin SR, van Kempen T, Li Y-C, Ponraj V, Nasajpour A, et al. Gold Nanocomposite Bioink for Printing 3D Cardiac Constructs. Advanced Functional Materials. 2017;27(12):1605352.
52. Jakus AE, Secor EB, Rutz AL, Jordan SW, Hersam MC, Shah RN. Three-Dimensional Printing of High-Content Graphene Scaffolds for Electronic and Biomedical Applications. ACS Nano. 2015;9(4):4636-48.
53. Theus AS, Ning L, Kabboul G, Hwang B, Tomov ML, LaRock CN, et al. 3D bioprinting of nanoparticle-laden hydrogel scaffolds with enhanced antibacterial and imaging properties. iScience. 2022;25(9):104947.
54. Szymański T, Semba JA, Mieloch AA, Cywoniuk P, Kempa M, Rybka JD. Hyaluronic acid and multiwalled carbon nanotubes as bioink additives for cartilage tissue engineering. Scientific Reports. 2023;13(1):646.
55. Pamies R, Cifre JGH, Espín VF, Collado-González M, Baños FGD, de la Torre JG. Aggregation behaviour of gold nanoparticles in saline aqueous media. Journal of Nanoparticle Research. 2014;16(4):2376.

56. Zare P, Aleemardani M, Seifalian A, Bagher Z, Seifalian AM. Graphene Oxide: Opportunities and Challenges in Biomedicine. Nanomaterials. 2021;11(5):1083.
57. Olate-Moya F, Rubí-Sans G, Engel E, Mateos-Timoneda MÁ, Palza H. 3D Bioprinting of Biomimetic Alginate/Gelatin/Chondroitin Sulfate Hydrogel Nanocomposites for Intrinsically Chondrogenic Differentiation of Human Mesenchymal Stem Cells. Biomacromolecules. 2024.
58. Naguib M, Kurtoglu M, Presser V, Lu J, Niu J, Heon M, et al. Two-Dimensional Nanocrystals Produced by Exfoliation of Ti3AlC2. Advanced Materials. 2011;23(37):4248-53.
59. Naguib M, Mashtalir O, Carle J, Presser V, Lu J, Hultman L, et al. Two-Dimensional Transition Metal Carbides. ACS Nano. 2012;6(2):1322-31.
60. Naguib M, Gogotsi Y. Synthesis of Two-Dimensional Materials by Selective Extraction. Accounts of Chemical Research. 2015;48(1):128-35.
61. Anasori B, Lukatskaya M, Gogotsi Y. 2D metal carbides and nitrides (MXenes) for energy storage. Nature Reviews Materials. 2017;2:16098.
62. Lyu B, Kim M, Jing H, Kang J, Qian C, Lee S, et al. Large-Area MXene Electrode Array for Flexible Electronics. ACS Nano. 2019;13(10):11392-400.
63. Seh ZW, Fredrickson KD, Anasori B, Kibsgaard J, Strickler AL, Lukatskaya MR, et al. Two-Dimensional Molybdenum Carbide (MXene) as an Efficient Electrocatalyst for Hydrogen Evolution. ACS Energy Letters. 2016;1(3):589-94.
64. Meixia X, Miaomiao LI, Song E, Haiyang S, Li Z, Jiaying BI. Halogenated Ti 3 C 2 MXene as High Capacity Electrode Material for Li-ion Batteries. Journal of Inorganic Materials. 2021;37:550.
65. Soleymaniha M, Shahbazi M-A, Rafieerad AR, Maleki A, Amiri A. Promoting Role of MXene Nanosheets in Biomedical Sciences: Therapeutic and Biosensing Innovations. Advanced Healthcare Materials. 2019;8(1):1801137.
66. Wu M, Yang J, Ye T, Wang B, Tang Y, Ying X. Efficient Drug Delivery of Ti3C2Tx MXenes for Synergistic Treatment of Human Hypopharyngeal Squamous Cell Carcinoma. ACS Applied Materials & Interfaces. 2023;15(25):29939-47.
67. Yang M, Wang L, Lu H, Dong Q. Advances in MXene-Based Electrochemical (Bio)Sensors for Neurotransmitter Detection. Micromachines. 2023;14(5):1088.
68. Lin H, Gao S, Dai C, Chen Y, Shi J. A Two-Dimensional Biodegradable Niobium Carbide (MXene) for Photothermal Tumor Eradication in NIR-I and NIR-II Biowindows. Journal of the American Chemical Society. 2017;139(45):16235-47.
69. Liu G, Zou J, Tang Q, Yang X, Zhang Y, Zhang Q, et al. Surface Modified Ti3C2 MXene Nanosheets for Tumor Targeting Photothermal/Photodynamic/Chemo Synergistic Therapy. ACS Applied Materials & Interfaces. 2017;9(46):40077-86.
70. Boularaoui S, Shanti A, Lanotte M, Luo S, Bawazir S, Lee S, et al. Nanocomposite Conductive Bioinks Based on Low-Concentration GelMA and MXene Nanosheets/Gold Nanoparticles Providing Enhanced Printability of Functional Skeletal Muscle Tissues. ACS Biomaterials Science & Engineering. 2021;7(12):5810-22.
71. Rastin H, Zhang B, Mazinani A, Hassan K, Bi J, Tung T, et al. 3D Bioprinting of Cell-Laden Electroconductive MXene Nanocomposite Bioinks. Nanoscale. 2020;12.
72. Asaro GA, Solazzo M, Suku M, Spurling D, Genoud K, Gonzalez JG, et al. MXene functionalized collagen biomaterials for cardiac tissue engineering driving iPSC-derived cardiomyocyte maturation. npj 2D Materials and Applications. 2023;7(1):44.

73. Lee SH, Kang MS, Jeon S, Jo HJ, Hong SW, Kim B, et al. 3D bioprinting of human mesenchymal stem cells-laden hydrogels incorporating MXene for spontaneous osteodifferentiation. Heliyon. 2023;9(3):e14490.
74. Alhabeb M, Maleski K, Anasori B, Lelyukh P, Clark L, Sin S, et al. Guidelines for Synthesis and Processing of Two-Dimensional Titanium Carbide (Ti3C2Tx MXene). Chemistry of Materials. 2017;29(18):7633-44.
75. Schneider CA, Rasband WS, Eliceiri KW. NIH Image to ImageJ: 25 years of image analysis. Nature Methods. 2012;9(7):671-5.
76. Dani S, Ahlfeld T, Albrecht F, Duin S, Kluger P, Lode A, et al. Homogeneous and Reproducible Mixing of Highly Viscous Biomaterial Inks and Cell Suspensions to Create Bioinks. Gels. 2021;7(4):227.
77. Cooke ME, Rosenzweig DH. The rheology of direct and suspended extrusion bioprinting. APL Bioengineering. 2021;5(1).
78. Gillispie GJ, Copus J, Uzun-Per M, Yoo JJ, Atala A, Niazi MKK, et al. The correlation between rheological properties and extrusion-based printability in bioink artifact quantification. Mater Des. 2023;233.
79. Tezel GB, Arole K, Holta DE, Radovic M, Green MJ. Interparticle interactions and rheological signatures of Ti3C2Tz MXene dispersions. Journal of Colloid and Interface Science. 2022;605:120-8.
80. Rastin H, Zhang B, Mazinani A, Hassan K, Bi J, Tung TT, et al. 3D bioprinting of cell-laden electroconductive MXene nanocomposite bioinks. Nanoscale. 2020;12(30):16069-80.
81. Zhu H, Dai W, Wang L, Yao C, Wang C, Gu B, et al. Electroactive Oxidized Alginate/Gelatin/MXene (Ti3C2Tx) Composite Hydrogel with Improved Biocompatibility and Self-Healing Property. Polymers. 2022;14(18):3908.
82. Natu V, Sokol M, Verger L, Barsoum MW. Effect of Edge Charges on Stability and Aggregation of Ti3C2Tz MXene Colloidal Suspensions. The Journal of Physical Chemistry C. 2018;122(48):27745-53.
83. Boularaoui S, Shanti A, Lanotte M, Luo S, Bawazir S, Lee S, et al. Nanocomposite Conductive Bioinks Based on Low-Concentration GelMA and MXene Nanosheets/Gold Nanoparticles Providing Enhanced Printability of Functional Skeletal Muscle Tissues. ACS Biomater Sci Eng. 2021;7(12):5810-22.
84. Akuzum B, Maleski K, Anasori B, Lelyukh P, Alvarez NJ, Kumbur EC, et al. Rheological Characteristics of 2D Titanium Carbide (MXene) Dispersions: A Guide for Processing MXenes. ACS Nano. 2018;12(3):2685-94.
85. Venkata Krishna D, Ravi Sankar M. Persuasive factors on the bioink printability and cell viability in the extrusion-based 3D bioprinting for tissue regeneration applications. Engineered Regeneration. 2023;4(4):396-410.
86. Jang J, Seol Y-J, Kim HJ, Kundu J, Kim SW, Cho D-W. Effects of alginate hydrogel cross-linking density on mechanical and biological behaviors for tissue engineering. Journal of the Mechanical Behavior of Biomedical Materials. 2014;37:69-77.
87. Malektaj H, Drozdov AD, deClaville Christiansen J. Mechanical Properties of Alginate Hydrogels Cross-Linked with Multivalent Cations. Polymers. 2023;15(14):3012.
88. Hodder E, Duin S, Kilian D, Ahlfeld T, Seidel J, Nachtigall C, et al. Investigating the effect of sterilisation methods on the physical properties and cytocompatibility of methyl cellulose used in combination with alginate for 3D-bioplotting of chondrocytes. Journal of Materials Science: Materials in Medicine. 2019;30(1):10.

89. Zhang W, Chen X, Wang Y, Wu L, Hu Y. Experimental and Modeling of Conductivity for Electrolyte Solution Systems. ACS Omega. 2020;5(35):22465-74.
90. Naseri Boroujeni S, Maribo-Mogensen B, Liang X, Kontogeorgis GM. New Electrical Conductivity Model for Electrolyte Solutions Based on the Debye–Hückel–Onsager Theory. The Journal of Physical Chemistry B. 2023;127(46):9954-75.
91. Alshwawreh N, Alhamarneh B, Altwarah Q, Quandour S, Barghout S, Ayasrah O. Electrical Resistivity and Tensile Strength Relationship in Heat-Treated All Aluminum Alloy Wire Conductors. Materials. 2021;14(19):5738.
92. Basmaciyan L, Azas N, Casanova M. Calcein+/PI- as an early apoptotic feature in Leishmania. PLoS One. 2017;12(11):e0187756.
93. Dai C, Lin H, Xu G, Liu Z, Wu R, Chen Y. Biocompatible 2D Titanium Carbide (MXenes) Composite Nanosheets for pH-Responsive MRI-Guided Tumor Hyperthermia. Chemistry of Materials. 2017;29(20):8637-52.
94. Dragan AI, Casas-Finet JR, Bishop ES, Strouse RJ, Schenerman MA, Geddes CD. Characterization of PicoGreen interaction with dsDNA and the origin of its fluorescence enhancement upon binding. Biophys J. 2010;99(9):3010-9.
95. Morwood AJ, El-Karim IA, Clarke SA, Lundy FT. The Role of Extracellular Matrix (ECM) Adhesion Motifs in Functionalised Hydrogels. Molecules. 2023;28(12):4616.
96. Bonetti L, De Nardo L, Farè S. Chemically Crosslinked Methylcellulose Substrates for Cell Sheet Engineering. Gels. 2021;7(3):141.
97. Zhang R, Zhang D, Sun X, Song X, Yan KC, Liang H. Polyvinyl alcohol/gelatin hydrogels regulate cell adhesion and chromatin accessibility. International Journal of Biological Macromolecules. 2022;219:672-84.

Acknowledgements – Yana H. is grateful for the learning opportunity provided by Roman A.P. and Miguel A.M.T. at Universidad de Catalunya in Barcelona, Spain. Special appreciation goes to Max J. for his supervision and guidance during the internship. Àngela Esplugues López is thanked for her additional guidance and her data on autoclavation. Dr. Eduardo Pérez del Rio (Universidad Politècnica de Catalunya, Barcelona, Spain) is gratefully acknowledged for his input in the electrical characterization.

Author contributions – Roman A.P. and Miguel A.M.T. conceived and designed the research. Yana H. conducted the experiments and analysed the corresponding data, with assistance from Max J.: Yana H. also wrote the paper. All authors carefully edited the manuscript.

SUPPLEMENTARY INFORMATION

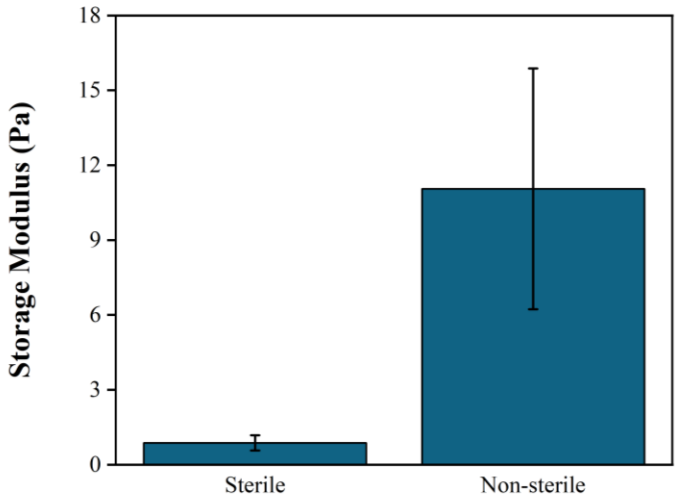

Fig. S1 – Effects of autoclavation on storage modulus of 1% w/v alginate 3% w/v gelatine hydrogels. Values in triplicates at 1% oscillation strain. Data: Àngela Esplugues López.

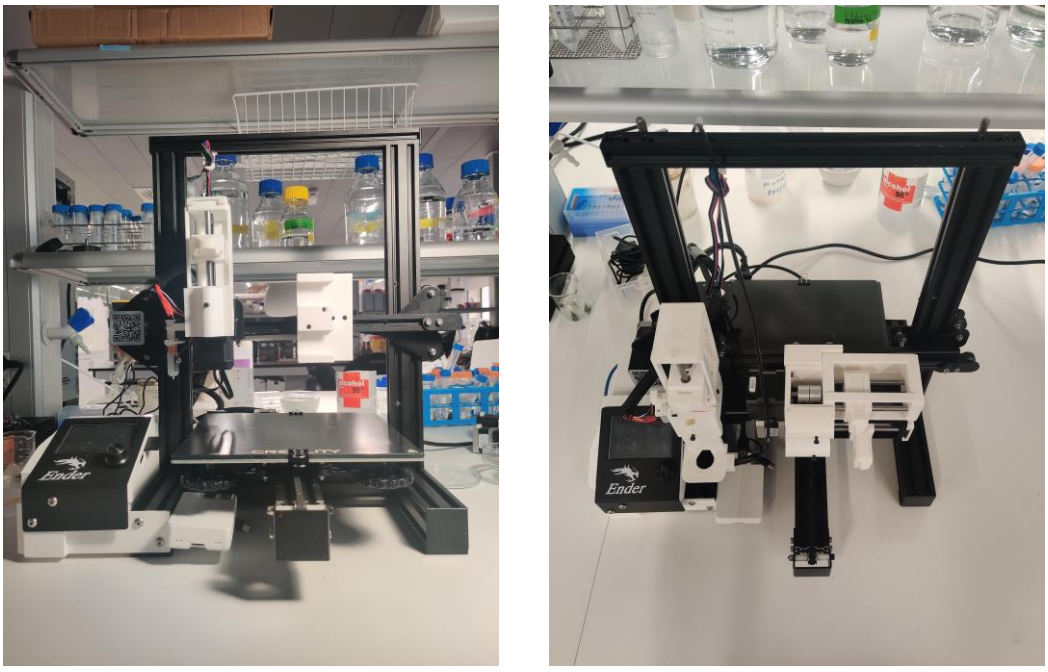

Fig. S2 – Bioprinter assembled by M. Jergitsch.

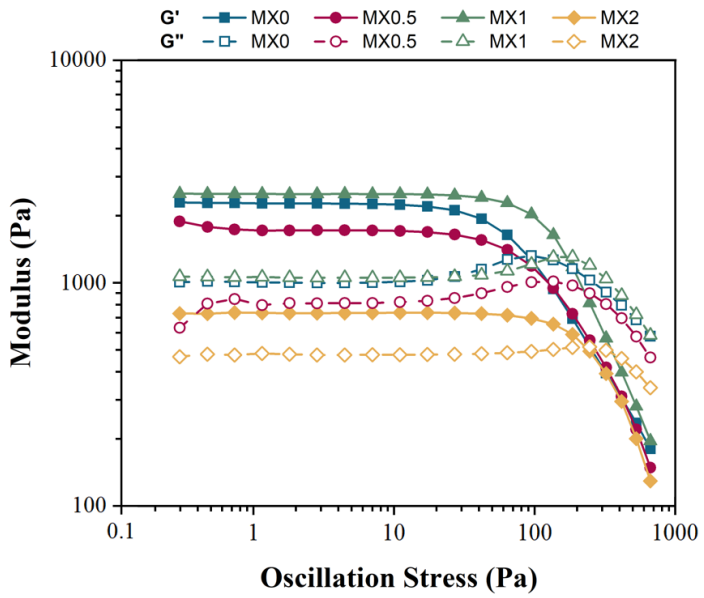

Fig. S3 – Linear viscoelastic region acquired from **a**mplitude sweep. G': storage modulus; G": loss modulus.

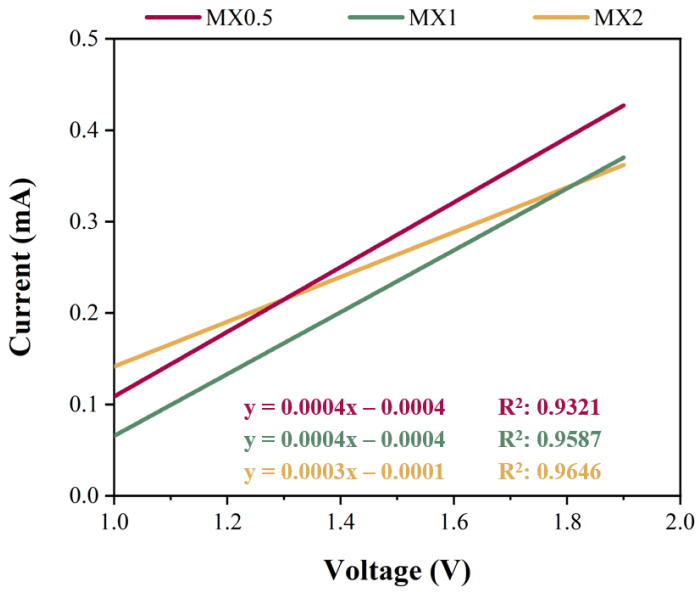

Fig. S4 – Linear approximation of I/V-curve between 1V and 1.9V.